Water Resources Research

RESEARCH ARTICLE
10.1029/2018WR024290

Equivalence of Discrete Fracture Network and Porous Media Models by Hydraulic Tomography

Yanhui Dong[1,2,3], Yunmei Fu[1,2,3], Tian-Chyi Jim Yeh[4,6], Yu-Li Wang[6], Yuanyuan Zha[5], Liheng Wang[1,2,3], and Yonghong Hao[4]

[1]Key Laboratory of Shale Gas and Geoengineering, Institute of Geology and Geophysics, Chinese Academy of Sciences, Beijing, China, [2]College of Earth and Planetary Sciences, University of Chinese Academy of Sciences, Beijing, China, [3]Institutions of Earth Science, Chinese Academy of Sciences, Beijing, China, [4]Key Laboratory for Water Environment and Resources, Tianjin Normal University, Tianjin, China, [5]State Key Laboratory of Water Resources and Hydropower Engineering Science, Wuhan University, Wuhan, China, [6]Department of Hydrology and Atmospheric Sciences, University of Arizona, Tucson, AZ, USA

Abstract Hydraulic tomography (HT) has emerged as a potentially viable method for mapping fractures in geologic media as demonstrated by recent studies. However, most of the studies adopted equivalent porous media (EPM) models to generate and invert hydraulic interference test data for HT. While these models assign significant different hydraulic properties to fractures and matrix, they may not fully capture the discrete nature of the fractures in the rocks. As a result, HT performance may have been overrated. To explore this issue, this study employed a discrete fracture network (DFN) model to simulate hydraulic interference tests. HT with the EPM model was then applied to estimate the distributions of hydraulic conductivity (K) and specific storage (S_s) of the DFN. Afterward, the estimated fields were used to predict the observed heads from DFN models, not used in the HT analysis (i.e., validation). Additionally, this study defined the spatial representative elementary volume (REV) of the fracture connectivity probability for the entire DFN dominant. The study showed that if this spatial REV exists, the DFN is deemed equivalent to EPM and vice versa. The hydraulic properties estimated by HT with an EPM model can then predict head fields satisfactorily over the entire DFN domain with limited monitoring wells. For a sparse DFN without this spatial REV, a dense observation network is needed. Nevertheless, HT is able to capture the dominant fractures.

Key Points:
- Spatial REV of fracture connectivity probability defines the equivalence of a discrete fracture network (DFN) and porous media
- For a highly dense DFN with spatial REV, hydraulic properties derived from hydraulic tomography predict independent flow fields well
- For a sparse DFN without a spatial REV, hydraulic tomography with an Equivalent Porous Media model captures large-scale dominant fractures

Supporting Information:
- Supporting Information S1

Correspondence to:
T.-C. J. Yeh,
yeh@hwr.arizona.edu

Citation:
Dong, Y., Fu, Y., Yeh, T.-C. J., Wang, Y.-L., Zha, Y., Wang, L., & Hao, Y. (2019). Equivalence of discrete fracture network and porous media models by hydraulic tomography. *Water Resources Research*, *55*, 3234–3247. https://doi.org/10.1029/2018WR024290

Received 18 OCT 2018
Accepted 11 MAR 2019
Accepted article online 21 MAR 2019
Published online 23 APR 2019

1. Introduction

Accurate prediction of fluid flow and mass transport in fractured geologic media is critical to water resources management, waste disposal/isolation, and hydrocarbon production. Various models for analyzing flow and transport in fractured rocks have been developed during recent decades (see review by Illman, 2014).

A fractured geologic medium consists of a mixture of solids and two distinct populations of voids: fractures and matrix pores. In fractured geologic media, fractures are the void population characterized by large and planar shape while matrix pores present a population consisting of voids of small and granular shapes. According to Yeh, Mao, et al. (2015), over the past decades, two conceptual models have emerged for characterizing and modeling the fractured media: (1) equivalent porous media (EPM) models and (2) discrete fracture network (DFN) models. The EPM assumes the two populations of pores are hydraulically connected, while DFN focuses on the fracture population only.

EPM approach is further divided into two groups: (a) the homogeneous model (EPM-homo) and (b) the heterogeneous model (EPM-hetero). The EPM-homo model is built upon the representative elementary volume (REV) concept (Bear, 1972). That is, it assumes that a rock mass has a sufficiently dense fracture network so that the hydraulic property defined over some control volume (CV; smaller than the entire rock mass) is independent of the spatial location of the volume. As such, the entire rock mass can be treated as a collection of a large number of CVs, which has the same hydraulic property, and the rock mass thus is homogeneous in terms of the hydraulic property. This CV is commonly called REV but is referred to as spatial REV in Yeh, Mao, et al. (2015) to distinguish it from the ensemble REV. The ensemble REV accommodates the situations in which the spatial REV does not exist but the rock mass is nonetheless treated as homogeneous. In other words, the REV (homogeneity) exists only in the ensemble sense in the stochastic context. In spite of the existence or nonexistence of spatial REV, effects of the contrast of the two void populations and distinctly

different responses between the fractures and the matrix in fractured rocks result in the use of the dual porosity or dual permeability model, EPM-dual (e.g., Illman & Hughson, 2005). The dual porosity model treats the matrix as a nonconducting storage reservoir while the latter allows the fracture and matrix to conduct and storage fluids (Illman, 2014). Both models, as an EPM-dual model, treat the entire fractured domain as two overlapping and interacting EPM-homo models, one for matrix and the other the fracture (i.e., two REVs): Each has an effective hydraulic property over the entire domain. Studies based on these models include Barenblatt et al. (1960), Warren and Root (1963), Duguid and Lee (1977), Bibby (1981), Moench (1984), Pruess and Narasimhan (1985), Dykhuizen (1990), Gerke and Vangenuchten (1993a, 1993b), Zimmerman et al. (1993), Reimus et al. (2003), and Roubinet and Irving (2014). Because of the homogeneity assumption over the entire fractured geologic medium, these two models are only suitable for describing overall flow and transport behaviors averaged over a large volume of fractured media, which often do not meet the resolution of our interest.

The demand for high-resolution predictions thus promoted the development of the EPM-hetero model. Without invoking the spatial REV assumption, this model uses small CV to define the hydraulic properties (eg., Neuman, 1987; Tsang et al., 1996) as we do in this study. It visualizes a fractured geologic medium as a collection of many small porous media blocks, each of which has a district hydraulic property. The rock mass, therefore, is considered heterogeneous. Likewise, DFN models idealize flow through a fractured rock mass as flow through an entity consisting of a collection of interconnected conduits (planar voids between two parallel plates) but omit flow through surrounding matrix (Cacas et al., 1990; Dershowitz & Einstein, 1988; Dverstorp et al., 1992; Long et al., 1982; National Research Council, 1996).

These conceptual models (EPM and DFN) all rely on the continuum and laminar flow assumption (i.e., Darcy's law is valid), which means both EPM models and DFN models have the same flow equation except that the DFN relates the coefficient of the linear relationship between specific discharge and the gradient to fracture characteristics such as aperture, length, and width (i.e., the cubic law). Therefore, to accurately model laminar flow in fractured rocks, the real challenge for either EPM or DFN lies on whether we can characterize the complex spatial pattern of fractures in details or not (Yeh, Khaleel, & Carroll, 2015).

One way to characterize the complex spatial pattern of fractures in details is to collect the hydraulic property at local scale using hydraulic tests at a large number of locations and then to estimate their distribution by interpolation methods such as kriging. This approach encounters two major difficulties: (1) insufficient local hydraulic property measurements and (2) the fact that the kriging interpretation relies on the statistical relationship between adjacent locations but it is not a true one. In order to overcome these difficulties, geophysical surveys, which could noninvasively deploy a large number of sensors cover a large area of the rock mass, could be a solution. They, nevertheless, often detect anomalies, which may not be related to fractures. In effect, the most intuitive approach for detecting fracture connectivity, which is the key to the flow and transport in fractured media, is cross-hole hydraulic interference tests.

During a hydraulic interference test, hydraulically connected wells, even kilometers far apart, can be easily detected (Illman et al., 2009; Zha et al., 2014, 2016). However, with limited monitoring wells and tests, the interference tests cannot pinpoint the connectivity spatial distribution if the number of wells is limited. As a consequence, applications of hydraulic interference tests in a tomography fashion (hydraulic tomography, HT) emerge as a viable solution, when only a limited number of wells are available. Briefly, HT is sequential pumping tests in a well field to collect non-fully-redundant information about the heterogeneity of the aquifer. That is, a well is pumped, and responses of other wells are collected, which are tantamount to a snapshot of the aquifer heterogeneity at one perspective at an angle. Then, the pumping test is conducted at another well, and drawdowns at the other wells are collected—another snapshot of the heterogeneity at a different perspective and angle. Therefore, by changing the pumping well location, many snapshots of the aquifer heterogeneity at different perspectives and angles can be acquired. Synthesizing all these snapshots leads to a more realistic mapping of aquifer heterogeneity than using one snapshot.

Over the past decades, the power of HT for mapping heterogeneity in porous media has been unequivocally demonstrated by many (Berg & Illman, 2011, 2013, 2015; Huang et al., 2011; Illman et al., 2012; Kuhlman et al., 2008; Liu et al., 2002, 2007, 2014; Tso et al., 2016; Wen et al., 2010; Ye et al., 2005; Zha et al., 2016; Zhu & Yeh, 2006). For mapping fractures in geologic media, encouraging HT results have been obtained in a few laboratory and field studies (Brauchler et al., 2003; Castagna et al., 2011; Illman, 2014; Illman

et al., 2009; Sharmeen et al., 2012; Zha et al., 2014, 2016), yet many more studies are necessary to further assess HT's viability.

Conducting many field experiments would be most logical for assessing the ability of HT for fractured geologic media, but the costs of the experiments always prohibit this undertaking. For this reason, synthetic numerical studies could be an alternative. In synthetic studies, the HT can be tested under a variety of conditions for different DFNs. While a few synthetic simulation studies of HT for characterization of hydraulic parameters of fractured rocks have been attempted (e.g., Castagna et al., 2011; Fischer et al., 2017, 2018; Hao et al., 2008; Ni & Yeh, 2008; Sharmeen et al., 2012; Wang et al., 2017; Zha et al., 2014, 2015), most of these studies adopted EPM-hetero models to describe fractures and to generate synthetic hydraulic interference test data for HT. These studies suggested that EPM-hetero models with high contrast in hydraulic parameters and fined grids appear to be appropriate for representing fractured geologic media. Nonetheless, they implicitly assume continuous hydraulic connectivity over the entire geologic media although fractures are hydraulically disconnected from the matrix. That is, the synthetic hydraulic data generated from EPM models may have predisposed HT with EPM-hetero model to successively simulate flow in fractured geologic media.

For the above reasons, the main objective of this paper is to understand the extent to which HT with EPM-hetero approach can characterize fracture networks generated by DFN models, which do not consider matrix. In order to accomplish this objective, three DFN models with different densities were randomly generated and were used to conduct multiple sets of injection hydraulic interference tests. Based on these synthetic data, transient HT was applied to characterize distributions of hydraulic parameters of EPM-hetero models, which are equivalent to conductivity and specific storage of the DFN. The meanings and values of the estimated hydraulic property distributions were then explored and validated by comparing the heads from the DFN model and EPM-hetero model at monitoring wells that were not used in the HT calibration. Moreover, a spatial REV concept in terms of probability of fracture connectivity was established for assessing the equivalence of EPM-hetero and DFN models. This spatial REV for the fracture connectivity probability refers to the likelihood (i.e., probability) that the fractures in a CV are connected is the same as that of other CV at any location in the domain. Notice that CVs with the same probability of connectivity do not necessarily have the same hydraulic properties. This spatial REV concept is different from the spatial REV for hydraulic properties (e.g., hydraulic conductivity, K), as discussed in previous paragraphs, which means the K value of the REV is representative of the entire domain in spite of the location of REV.

Lastly, the REV sizes of DFN models densities were discussed to explore their impacts on the performance of HT in fractured media.

2. Design of DFN Models

2.1. Fracture Generation

In order to investigate the performance of HT in different types of fracture networks, three DFNs (models A, B, and C) with a different fracture intensity were randomly generated using the FracMan software (Golder Associates Inc, 2015); see Figure 1. For the sake of simplification, we mainly focus on two-dimensional DFNs in the study.

A domain size of 1,000 m (x) × 1,000 m (y) × 1 m (z) was used in each DFN model. Considering that the thickness is negligible compared to the horizontal size, the DFN models can be considered as two-dimensional models. Each model consisted of two sets of small fractures (Set1 and Set2) and two faults (F1 and F2). The total fracture number of Set1 and Set2 in models A, B, and C were 200, 500, and 1,000, respectively. The geometrical and hydraulic parameters used in the DFN models are listed in Table 1. The parameters for all fractures in each set were kept constant. The Enhanced Baecher Model (Baecher et al., 1977) was employed to generate the locations of fracture centers based on a Poisson process (Golder Associates Inc, 2015). All fractures were generated as vertical square planes at the center locations according to the equivalent radius in Table 1. The area of the square is the same as the area the circle of this given radius. The fractures may be truncated by the other fractures or the model surfaces, which form the final fractures of different lengths as shown in Figure 1. The effect of geometrical parameters was not investigated in the study since the emphasis was the effect of the fracture intensity of the DFN models.

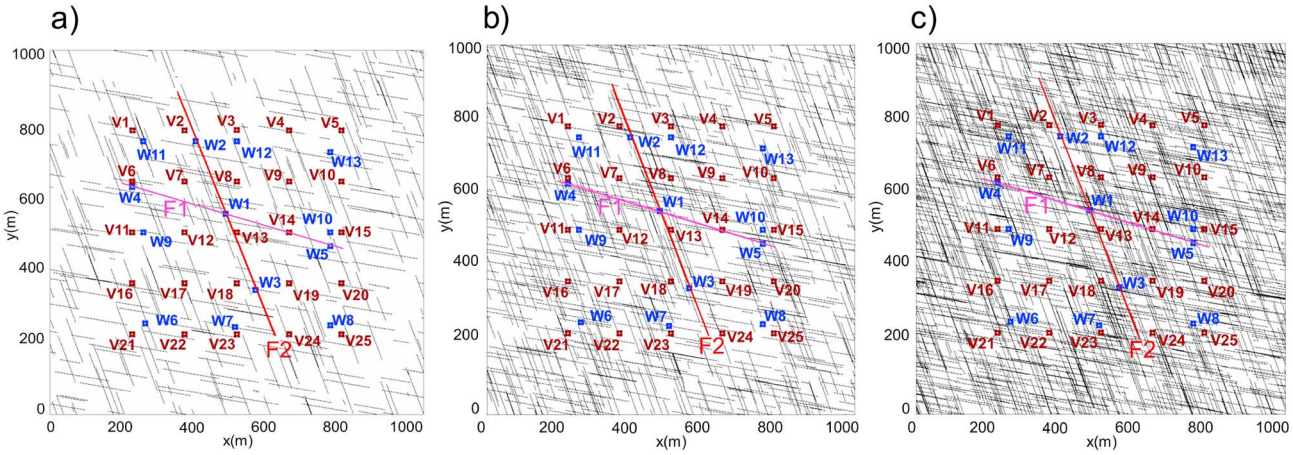

Figure 1. Plan view in the *XY* plane of the synthetic discrete fracture network models with different intensity. The blue wells (W1–W13) were used in inverse modeling, while the red ones (V1–V25) were used for independent validation. The red lines are faults F1 and F2. (a) Model A, fracture number = 200; (b) model B, fracture number = 500; (c) model C, fracture number = 1,000.

2.2. Synthetic Injection Tests Used for Inversion and Validation

To generate data for inversion, 13 wells were placed in the DFN models, and five of which are located on F1/F2, while the rest are roughly evenly distributed in the central region of the model. Every well was located at one fracture, at least, and fully penetrates the fracture plane. A sequential injection at selected nine wells (W1–W6, W8, W9, and W12) was simulated to obtain groundwater head responses at all wells. The injection rate was 0.00001 m^3/s for a duration of 150 hr.

For objectively assessing the robustness of the estimated K and S_s tomograms?25 new validation wells (V1–V25, Figure 1) were placed evenly in the DFN models with an interval of 140 m. Because of the discrete nature of the fractures, these wells may not locate exactly at the generated fractures. In order to avoid this problem, we assumed that if a fracture was within the 5-m radius of a validation well, the well was moved to the closest fracture; otherwise, the well remained disconnected with any fracture. According to this principle, there were 5 validation wells connected to fractures in model A (V4, V6, V13, V14, and V16), 17 validation wells were located at fractures in model B (wells except for V4, V7, V10, V15, V17, V23, V24, and V25), and 19 validation wells in model C (wells except for V10, V18, V20, V21, V22, and V24).

A sequential injection at three center-located validation wells (V12, V13, and V14) was simulated to obtain groundwater head responses at other wells. Eleven data points from each injection response time series were selected to represent the observed data for validation. The corresponding predicted water head responses based on the estimated K and S_s were compared with those observed to validate HT. Note that the use of new validation wells avoids the reciprocity issue if any.

2.3. Numerical Simulation of Groundwater Flow in DFN Models

Transient groundwater flow simulation was conducted with the generated 3-D DFN. The governing equation for two-dimensional flow in a fracture is described by

Table 1
Geometrical and Hydraulic Model Parameters Used in DFN Models

	Orientation (degree) Strike	dip	Equivalent radius (m)	Aperture (m)	Permeability (m^2)	Compressibility (1/kPa)
Set1	170	90	70	0.01	9.87E–12	1.00E–07
Set2	100	90	70	0.005	2.96E–12	1.00E–07
F1	165	90	300	0.03	9.87E–11	1.00E–07
F2	105	90	400	0.02	3.95E–11	1.00E–07

Note. DFN = discrete fracture network.

$$S\frac{\partial h}{\partial t} - T\nabla^2 h = q, \tag{1}$$

$$T = Kb = \frac{k\,\rho g b}{\mu}, \tag{2}$$

where S is fracture storativity (dimensionless), h is the hydraulic head (L), T is fracture transmissivity(L^2/T), q is source/sink term (L/T), t is time(T), ∇^2 is the 2-D Laplace Operator, k is fracture permeability (L^2), ρ is fluid density (M/L^3), g is the gravitational acceleration(L/T^2), b is fracture aperture (L), and μ is fluid viscosity (M/[L·T]). These equations assume laminar flow in the fractures.

The planar fractures were subdivided into small triangular elements, and the MAFIC program (Miller et al., 2001) was used to calculate the head distributions in the fractures. The initial hydraulic head distribution was spatially uniform with a value of 100 m, and all the boundaries were set as no flux boundary. We emphasize that this simulation does not include any matrix, which surrounds the fractures in real-world scenarios.

3. Transient HT of Synthetic Data

3.1. Inverse Modeling Approach

Transient HT analysis of the synthetic injection test data from DFN models was conducted using the Simultaneous Successive Linear Estimator (SimSLE) algorithm (Xiang et al., 2009). SimSLE can estimate the K and S_s distributions as well as their uncertainties by taking all the available pumping/injection test data simultaneously instead of incorporating data sequentially into the estimation as is done in the Sequential Successive Linear Estimator (Zhu & Yeh, 2005).

3.2. Inverse Model Setup

The transient HT analysis was performed using the VSAFT2 code (Yeh et al., 1993), which includes the SimSLE algorithm. VSAFT2 is a 2-D finite element model, which solves flow and solute transport in heterogeneous geologic formations under variably saturated conditions. It is considered as a porous media model since it assumes spatial continuity in parameters and responses, although it can be used to simulate flow through fractured media by fine discretization of the fractures and by assigning large contracts between fractures and matrix properties.

Consistent with the DFN models generated previously, a 1,000 m × 1,000 m domain was used for each inverse model in VSAFT2. As a continuous mode (we will call it an equivalent porous media model, EPM, because it is used to mimic the behavior of the DFN model), the VSAFT2 model domain was discretized into 50 × 50 (2,500) square elements of 20 × 20 m^2 in size. The same boundary and initial conditions as those DFN models were used in the VSAFT2 models. For each injection response data series, four data points were selected in inversion: one for the early-time response (slowly varying buildup slope), two for intermediate-times (fast-varying buildup slope), and one for a late-time response (slowly varying buildup slope).

Computational requirements of simultaneous inversion of the injection tests using SimSLE can be significant. To conduct the transient HT efficiently, all the inversions were run on the Tianhe-2 supercomputer located in the National Supercomputer Center in Guangzhou, China. For each simulation, 24 to 48 threads were used on one or two computing nodes (each node has two Intel Xeon E5-2692 CPUs and 64 GB memory), which ensure that each simulation was completed in 1 hr.

4. Results From Transient HT and Validation

4.1. The Sparse DFN Model (Model A)

Figure 2a is the K tomogram (the perturbation of natural logarithm of K after removing the mean) based on EPM using HT with the injection data from DFM model A, while Figure 2c is the residual variance map of $ln\,K$ corresponding to the K tomogram. In the figures, the white circles represent the wells generating injection data. The red lines are the large fractures (F1 and F2), while the black lines are small fractures in the domain. The two white dash lines on Figures 2a and 2b outline the two fracture clusters in model A. As indicated in Figure 2a, the estimated high K region is mainly distributed along F1 and F2, accompanied by slightly high K zones at the regions with more connected fractures. The figures also reveal a low K zone, which separates the

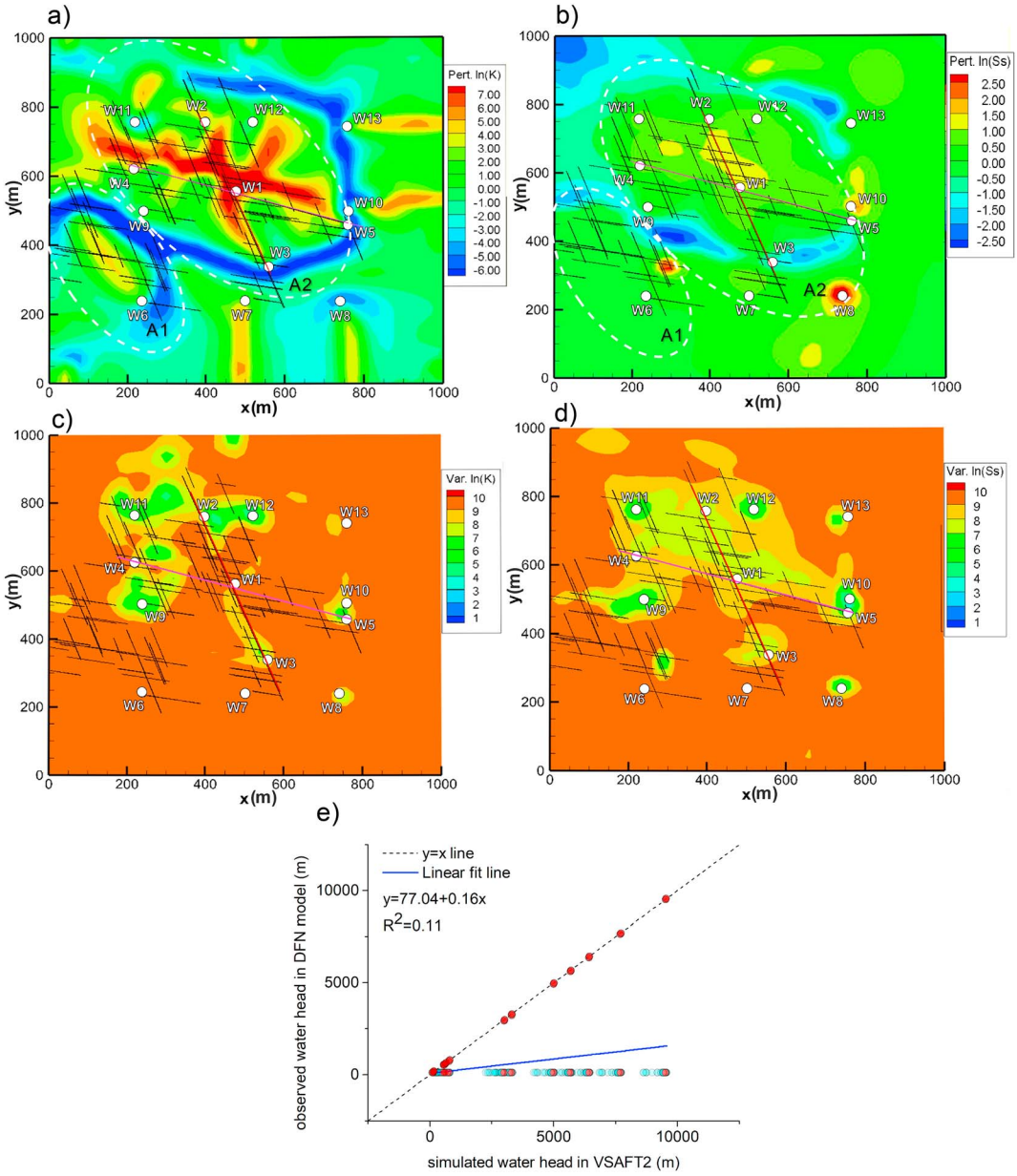

Figure 2. *K* and S_S tomograms estimated using synthetic data from model A and its validation. (a) *K* tomogram with all connected fractures; (b) S_S tomogram with all connected fractures; (c) estimated *ln K* residual variance map; (d) estimated *ln* S_S residual variance map; (e) validation results. DFN = discrete fracture network.

two independent fracture clusters (A1 and A2, surrounded by the white dashed lines). The results indicate that EPM has captured the difference in head response between W6 and the others in cluster A2. The *ln K* residual variance (Figure 2c) shows that the uncertainties around the wells are low; slightly low uncertainties also exist along some connected fractures and close to the estimated low *K* zones.

Figure 2b is the S_s tomogram, while Figure 2d is the estimated ln S_s residual variance map of the tomogram. In the forward DFN model, a uniform value of S_s was assigned to all fractures, which are discrete, and DFN assumes the absence of matrix. On the other hand, VSAFT2 used in SimSLE assumes a continuous geologic medium (EPM, including fractures and matrix). For this reason, higher values of the estimated S_s generally locates in the area with connected fractures where high *K* were identified, and low S_s estimates are associated with low *K* zones, although the contrast of the estimated S_s field is relatively small. This anomaly contradicting the common knowledge of high *K* and low S_s values for the fracture manifests the impact of the

use of coarse grids in VSAFT2 (an EPM) to imitate the flow behavior in the DFN model, which does not consider the matrix.

The scatter plot in Figure 2e is the validation result, which compares the total 792 pairs (three sets of head responses at 11 different times at 24 wells) of the observed heads in DFN and simulated heads based on the estimated parameters of the EPM. Red circles in the plot represent the heads at validation wells connected to fractures, while the light blue ones are the heads at the remaining validation wells. Since a large number of data points are overlapped, only a limited number of points are visible in the scatter plot. According to this figure, only a small number of data points fall on the 1:1 line while most are overpredicted by EPM (i.e., it predicts responses at locations where no responses are observed in DFN). This clearly indicates that connectivity between some injecting and monitoring wells was not fully resolved.

4.2. The Medium-Intensity DFN Model (Model B)

Similar to the results for Model A, Figure 3a shows that the estimated high K region is mainly distributed in the cross area of F1 and F2, especially along F1, which has the highest K and largest aperture. The dense fractures along both sides of F1 may contribute to the high K zone. Other identified high K zones (light yellow zones) are also consistent with the distributions of the connected fractures. Generally, lower uncertainties locate roughly around the wells from Figure 3c. With regard to the estimated S_s field, higher values are distributed in around the area of F1 and F2, covering a greater area in comparison with that in model A. This is consistent with the greater fracture zones in this area.

The validation result, a scatter plot of the total 792 pairs (three sets of head responses at 11 different times at 24 wells) of observed and simulated water heads, is illustrated in Figure 3e. Comparing the result with that of Mode A (Figure 2e), more data points, in this case, dispersed around the 1:1 line with relatively small bias, suggesting that the estimated K and S_s distributions of EPM roughly agree with the fracture distribution of the DFN model over the entire domain. There are still some overestimated data points, which are from the validation wells not located at the fractures, indicating that the HT with EPM was not able to yield low-permeability zones to isolate these wells from fractures.

4.3. The High-Intensity DFN Model (Model C)

According to Figure 4a, the estimated high K region is again mainly distributed along F1 and F2, as well as some region with densely connected fractures. A circular low K zone appears surrounding the high K zone due to the effect of the no-flux boundary used in the models. The area of low uncertainty region (Figure 4c) is much larger than those of models A/B. This is likely attributed to the fact that the fracture intensity of Model C is so large that the model is close to a porous medium model, and as a result, more information about heterogeneity and connectivity can be sampled during injection tests. With regard to S_s, values higher than that of actual fractures remain around F1, F2, and the connected fractures. However, much larger values S_s appear near the impermeable boundaries, reflecting that the injected water has migrated to the boundaries of the DFN in this case than in the other two cases, in addition to the reason discussed in section 4.1.

The scatter plot of the total 792 pairs (three sets of head responses at 11 different times at 24 wells) of observed and simulated water heads for the validation is shown in Figure 4e. Compared it with those of models A and B, much more data points cluster around the 1:1 line with small dispersion and bias, suggesting that the estimated K and S_s tomograms of EPM are close to the hydraulic properties of the DFN model. Nevertheless, heads at the five nonconnected validation wells were overpredicted (light blue circles). On the other hand, the simulated heads at V12 (a validation well not connected to fractures) agree well with the observed heads, indicating that SimSLE has captured the unconnected feature and translated it into low K zones.

Notice that all the locations of the low residual variances of the three cases do not follow exactly the patterns of the detected high conductivity zones. This should be expected since the residual variance, or analogous to the resolution matrix used by other inverse models (Zhang & Thurber, 2007), is an ensemble concept, which indicates the "likely" uncertainty (or unresolved heterogeneity) at the given location. This result reflects the fact that sparse head information alone will not pinpoint the locations of the high or low K zones. With a sparse monitoring network, additional information such as flux measurements could be beneficial (Tso et al., 2016; Zha et al., 2014).

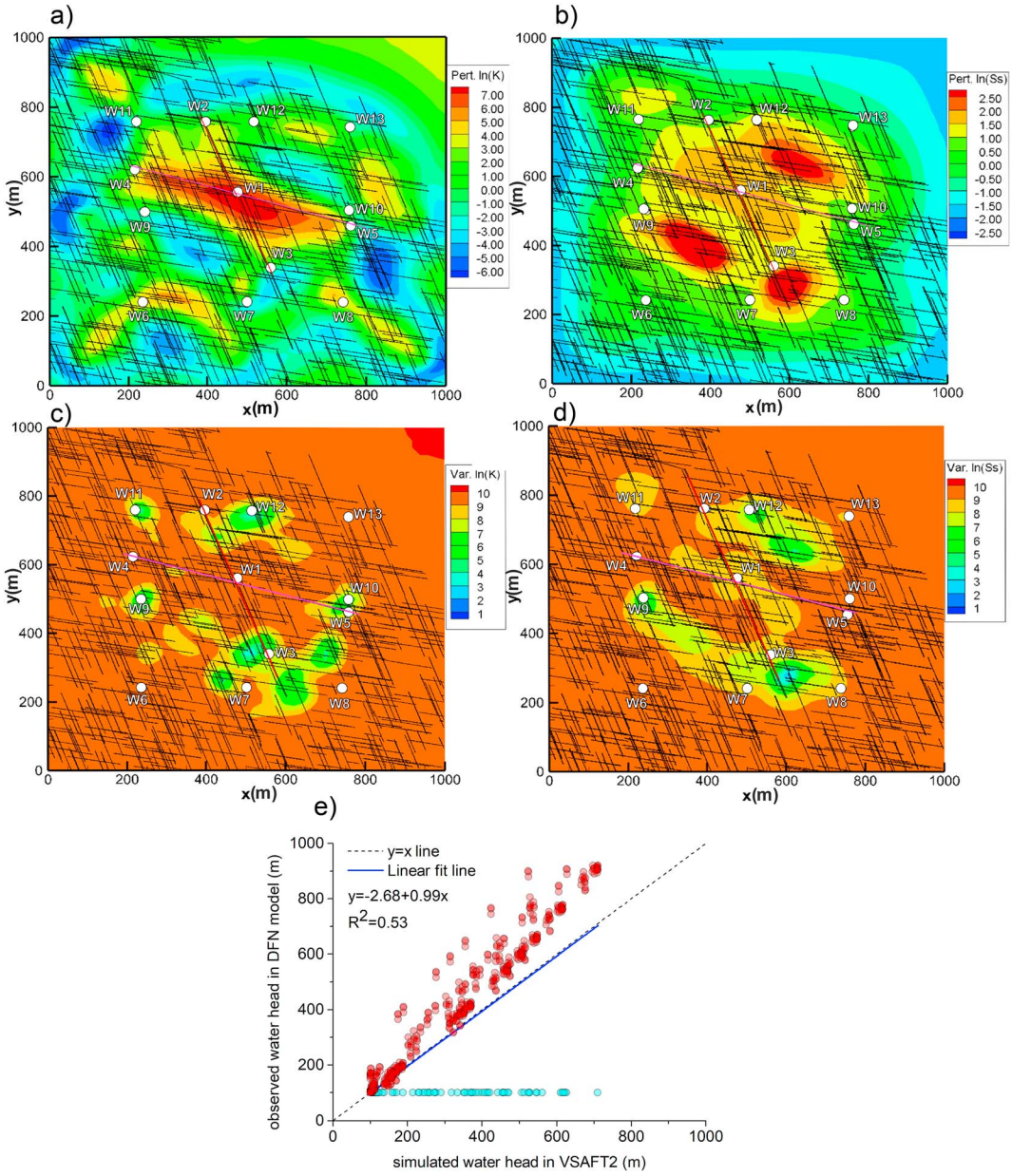

Figure 3. K and S_S tomograms estimated using synthetic data from model B and its validation. (a) K tomogram with all connected fractures; (b) S_S tomogram with all connected fractures; (c) estimated $ln\ K$ residual variance map; (d) estimated $ln\ S_S$ residual variance map; (e) validation results: scatter plots of observed water heads in model B and simulated ones in VSAFT2 based on the estimated K and S_S. The white circles represent the wells generating injection data. The red lines are the large fractures (F1 and F2), while the black lines are connected fractures extracted from all he fractures in the domain. Red circles repent validation wells connected to fractures, while light blue ones are the rest validation wells. DFN = discrete fracture network.

5. Discussion

Notice that the head (state variable) and T and S fields (parameters) of EPM-hetero model and DFN model, that is, equations (1) and (2), are not identical in theory. This is owing to the fact that the CV embedded in DFN model represents a volume much larger than many fluid molecules but smaller than the fracture void and these CVs are confined to fractures. On the other hand, the CV in the EPM-hetero model includes many fluid molecules, fractures, and pores in the matrix. The CVs for DFN and EPM are also different mathematically: One represents the parameters and state variable strictly in fracture domain, and the other represents those in EPM-hetero model, which are affected by both the matrix and fractures at various degrees. For instance, the head in the EPM-hetero model is influenced by both fractures and the matrix due to

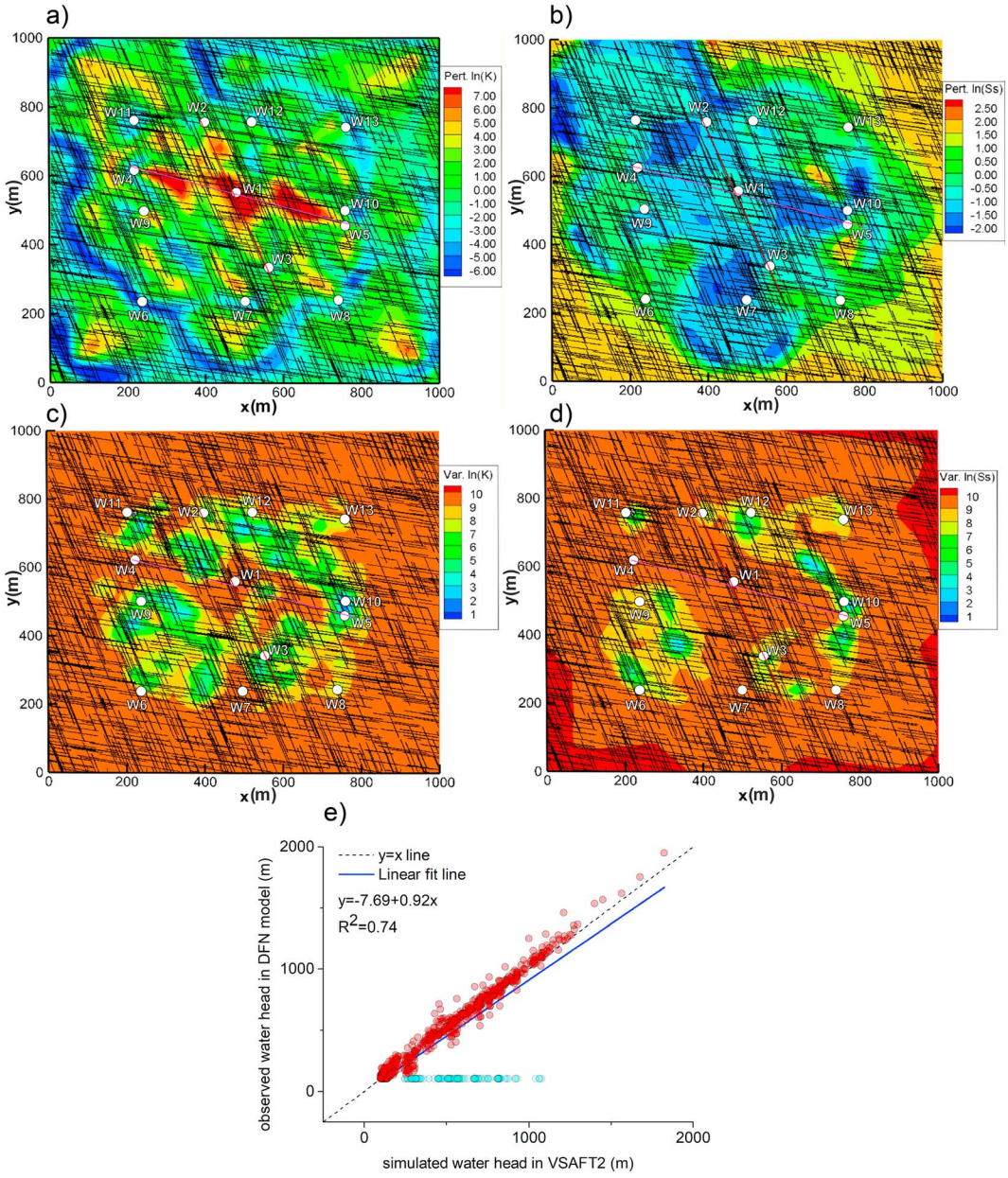

Figure 4. K and S_S tomograms estimated using synthetic data from model B and its validation. (a) K tomogram with all connected fractures; (b) S_S tomogram with all connected fractures; (c) estimated $ln\ K$ residual variance map; (d) estimated $ln\ S_S$ residual variance map; (e) validation results: scatter plots of observed water heads in model C and simulated ones in VSAFT2 based on the estimated K and S_S. The white circles represent the wells generating injection data. The red lines are the large fractures (F1 and F2), while the black lines are connected fractures extracted from all the fractures in the domain. Red circles repent validation wells connected to fractures, while light blue ones are the rest validation wells. DFN = discrete fracture network.

continuity in the governing equation. While these differences are deemed minor for the purpose of this study, we like to emphasize that the estimated parameter fields, based on SimSLE and the EPM-hetero model, are not those associated with DFN model but are conditional effective parameter fields (Yeh et al., 1996) that can reproduce observed well-hydrographs at the observation wells during all the injection tests. This should also explain the amorously large values of S_s for EPM elements that include or are near fractures, as discussed in section 4.1. In order to substantiate the usefulness of these estimated parameters, validation experiments were conducted to show that these parameter fields and model can predict transient head behaviors simulated by the DFN model during independent pumping tests.

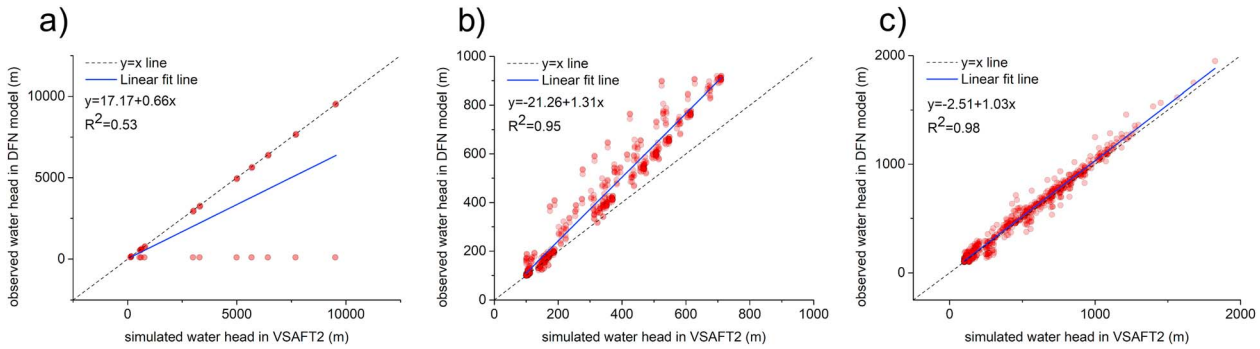

Figure 5. Validation results of validation wells connected to fractures: scatter plots of observed water heads in discrete fracture network (DFN) models and simulated ones in VSAFT2 based on the estimated K and S_S. (a) Model A; (b) model B; (c) model C.

From the validation results of the EPM for the DFN domains with different fracture intensities, we observe that the predicted heads by EPM parameters (based on HT) had a better performance in the DFN models with high fracture intensities such as models B and C. Since the isolated validation wells in DFN models have no responses during the injection tests, the head distribution has a bimodal distribution with two distinct populations: the heads at the wells in DFN, which have no responses, and the heads in those wells with some responses. The two populations were analyzed separately. The number of nonresponse wells in DFN, whose response were misinterpreted by the EPM model, is 20, 8, and 5 in models A, B, and C, respectively. As expected, the higher the fracture intensity, the less number of wells are isolated, and EPM is appropriate.

For the other population, in which some responses were observed, the assessment of K and S_s fields of EPM for predicting heads at the responding wells are illustrated in Figure 5. In Figure 5a, the head data from five validation wells connected to fractures in DFN are plotted against the corresponding heads predicted using EPM based on the HT analysis. As shown in the figure, the heads at V4 is significantly overpredicted by the EPM (the horizontal red circles) while the predicted heads using EPM and observed heads at the other four wells in DFN fall on the 1:1 line. This is due to the fact that although V4 is connected to a fracture within its 5-m radius zone, the fracture belongs to a local isolated fracture cluster. In addition, the SimSLE was not able to create a low K zone around the well due to the scarcity of monitoring wells. Even for the connected validation wells, the estimation of K and S_s of sparse DFN still has huge uncertainties. In Figure 5b, we observe that most data points from the 17 connected validation wells scattered around the upside of the 1:1 line, indicative of some bias. Overall, it seems that the estimation has been improved in comparison with that of model A. That is, head responses in DFN are captured by the EPM. In Figure 5c, all the data points from the 19 connected validation wells disperse along the 1:1 line with smaller bias compared with those of model B, indicating that the performance of HT by EPM has been improved significantly due to the connectivity feature resulting from the increase of fracture intensity of DFN model.

The validation results of the EPM for the three DFN models are illustrated in Table 2, through which we also found that both of absolute mean error and standard deviations decrease with the increasing fracture intensity of DFN models.

These results manifest that the sparseness of the DFN can significantly affect the predictability of flow in DFN using the EPM models. To further explore this effect, analysis of the spatial REV (Yeh, Mao, et al., 2015) in terms of fracture intensity was conducted. That is, a sequential sampling process with different sizes of the CV (i.e., $50 \times 50 \times 1$ m^3, $100 \times 100 \times 1$ m^3, $200 \times 200 \times 1$ m^3, $250 \times 250 \times 1$ m^3, $333 \times 333 \times 1$ m^3, and $500 \times 500 \times 1$ m^3) was undertaken on the DFN models (A, B, and C). That is, by moving the CV over the domain, avoiding the boundary, the fracture intensity (P_{32}, the total area of fractures per unit volume, Dershowitz & Herda, 1992; Grenon & Hadjigeorgiou, 2012) of each CV was calculated. Subsequently, the coefficient of variation (COV) of P_{32} was plotted with respect to the CV size, and the regression function was determined as shown in Figure 6. The spatial REV size was determined based on the values of COV of P_{32} in between

Table 2
Validation Error of Different Models

DFN models	Model A	Model B	Model C
Absolute mean error	967.21	83.66	38.68
Standard deviation	2234.23	78.81	38.70

Note. DFN = discrete fracture network.

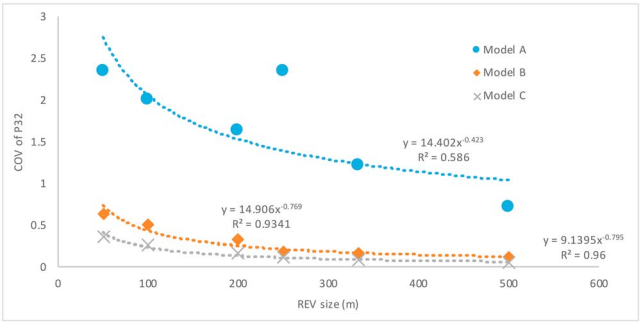

Figure 6. Coefficient of variation (COV) of P_{32} versus representative elementary volume (REV) size.

0.2 and 0.1 (Farichah et al., 2017; Grenon & Hadjigeorgiou, 2012). For model A (Figure 6), the COV of P_{32} fluctuates, and its variation remains significantly even with the increase in the CV size. Its minimum value is about 0.71, indicating that the fracture distribution in model A is localized and no spatial REV for fracture connectivity probability or spatial continuity exists. On the contrary, for models B and C, the COVs of P_{32} decrease (from 0.5 to 0.1) with the increase of the CV size. These results imply that in model B, if we arbitrarily choose a CV of a size of 250 × 250 × 1 m in any part of the domain, we find a COV of P_{32} about 0.14, indicating that the number of connected fractures within this CV is similar everywhere in model B. That is to say, the spatial REV for the number of fractures in model B is around 250 m. Likewise, the size of the spatial REV is around 200 m with a corresponding COV of P_{32} value of 0.16.

Determination of the REV using such a manual sampling approach can be very time-consuming, and it can only give a rough range of REV size. Farichah et al. (2017) investigated the parameters affecting the COV of P_{32} through synthetic DFN simulations and proposed an equation for determination of geometrical REV (a term used in geotechnical engineering for media with homogeneous fracture geometrical properties), which is

$$\text{COV of } P_{32} = 0.84 \times V^{-0.5} P_{32}^{-0.5} D, \tag{3}$$

where V is the volume of the CV (L^3), P_{32} is fracture intensity (L^{-1}) defined by the total area of fractures per unit volume in the CV and D is fracture equivalent diameter (L), defined by the diameter of the circle with an area equal to the area of the polygon describing the fracture plane, over the CV. Considering that more probably of fracture connectivity with larger P_{32}, the COV of P_{32} can also be used to calculate the size of spatial REV. Table 3 shows the spatial REV size calculated based on the manual approach as well as that using a COV of 0.15 from the above equation. As indicated in Table 3, the spatial REV size calculated using equation (3) is very close to those based on the manual approach, indicating the robustness of the equation.

Based on the above spatial REV analysis, the REV size apparently decreases with the increasing fracture intensity of DFN models. Although the spatial REV here is defined on the basis of geometrical properties of the fractures in a CV, it is equivalent to that in terms of hydraulic connectivity (the probability of having connected fractures; not the hydraulic conductivity). In addition, the analysis informs us that a spatial REV in terms of P_{32} exists in models B and C and not in model A. Implicitly, this result means that in the fracture network of models B and C, the probability that fractures are connected within the CV everywhere in the entire domain is the same and high. In other words, the entire domain with fracture systems of models B and C likely can be treated as a continuous network (EPM). This may be the reason for the good validation of the EPM parameters for the entire domain under models B and C. As an additional note, the entire model A domain, nevertheless, can be considered as an ensemble REV (Yeh, Mao, et al., 2015). That is, the P_{32} value is representative of the entire domain, and the requirement of the elementary volume is met in the ensemble sense since the entire DFN domain is merely one possibility (element) of the specified P_{32} value. Thus, the COV of P_{32} over the entire domain could be very large, and prediction uncertainty is large, which also explains the poor performance of the EPM, even using HT.

Table 3
REV Sizes Determined From Manual Statistic and Equation (3)

DFN model		Model A	Model B	Model C
REV size (m)	by manual statistic	none	~250	~200
	by Equation (3)	1058 (> domain size)	231	206

Note. DFN = discrete fracture network; REV = representative elementary volume.

Accordingly, we may conclude that for a sparse DFN system without a spatial REV such as model A, local fractures can be identified through the high K zone of the EPM by HT but the estimated distribution K and S_s over the entire DFN domain likely are not representative of the fracture network over the domain. An accurate mapping of a sparse DFN model requires extremely a high density of monitoring wells. On the other hand, in the case of DFNs with high fracture intensities, not only the representative fractures can be characterized but also a reasonable distribution of K and S_s of EPM can be obtained, which can be referred to as fracture zones, through limited number of monitoring wells (Zha et al., 2014, 2016).

6. Conclusions

The major findings and conclusions are as follows. We have developed a spatial REV concept in terms of fracture intensity (the probability of having connected fractures). This concept defines the equivalence between a DFN model and a porous medium model. If the spatial REV exists, a DFN model can be treated as an EPM and otherwise.

For a sparse DFN model without a spatial REV, only the dominant fractures can be identified by EPM by HT as high K zones, using a limited number of wells. Accurate mapping of individual fractures in a sparse DFN demands an extremely dense monitoring network. In the case of DFN models in which a spatial REV of fracture connectivity probability exists, not only the dominant fractures can be characterized but also a reasonable distribution of K and S_s (fracture zones) can be obtained through a limited number of wells with HT.

The spatial REV concept is very important for the characterization of fractured media. Equation (3) might provide a way to determine spatial REV through rough estimation of P_{32} and fracture equivalent diameter through fracture measurements. However, this approach remains a challenge to determine the REV size in practice since it requires a large number of measurements. The traditional spatial REV for defining homogeneous hydraulic properties of porous media faces the same difficulty. They are, nevertheless, useful for theoretical analyses.

Lastly, we emphasize that the study uses DFN to generate fracture networks to imitate real-world fractured geologic media. However, these fracture networks by DFN completely ignore the surrounding rock matrix. This omission of the matrix may exaggerate the discontinuity of the real-world fractured rock mass and inflate the difficulties for characterizing fractured rock mass in nature.

Acknowledgments
This research is financially supported by the National Science and Technology Major Project of China (Grant 2017ZX05008-003-021). Partial support was also provided by the Strategic Priority Research Program of the Chinese Academy of Sciences (Grant XDB10030601) and the Youth Innovation Promotion Association of the Chinese Academy of Sciences (Grant 2016063). T.-C. Jim Yeh also acknowledges supports from US Civilain Research and Development Foundation (CRDF) under the award number (DAA2-15-61224-1): Hydraulic tomography in shallow alluvial sediments: Nile River Valley, Egypt. He also acknowledges the Global Expert award through Tianjin Normal University from the Thousand Talents Plan of Tianjin City. Finally, we wish to thank Golder Associates Inc. for the support of using the FracMan software. The authors thank the editors and anonymous reviewers for their helpful and insightful comments, which have significantly improved this work. The program and the data used in this study can be achieved online (doi: 10.5281/zenodo.2544573).

References

Baecher, G. B., Lanney, N. A., & Einstein, H. H. (1977). Statistical description of rock properties and sampling. 18th U.S. Symposium on Rock Mechanics, 5C1–5C8.

Barenblatt, G. I., Zheltov, I. P., & Kochina, I. N. (1960). Basic concepts in the theory of seepage of homogeneous liquids in fissured rocks. *Journal of Applied Mathematics & Mechanics*, *24*(5), 1286–1303. https://doi.org/10.1016/0021-8928(60)90107-6

Bear, J. (1972). *Dynamics of fluids in porous media*. New York: American Elsevier Pub. Co.

Berg, S. J., & Illman, W. A. (2011). Three-dimensional transient hydraulic tomography in a highly heterogeneous glaciofluvial aquifer-aquitard system. *Water Resources Research*, *47*, W10507. https://doi.org/10.1029/2011WR010616

Berg, S. J., & Illman, W. A. (2013). Field study of subsurface heterogeneity with steady-state hydraulic tomography. *Ground Water*, *51*(1), 29–40. https://doi.org/10.1111/j.1745-6584.2012.00914.x

Berg, S. J., & Illman, W. A. (2015). Comparison of hydraulic tomography with traditional methods at a highly heterogeneous site. *Ground Water*, *53*(1), 71–89. https://doi.org/10.1111/gwat.12159

Bibby, R. (1981). Mass-transport of solutes in dual-porosity media. *Water Resources Research*, *17*(4), 1075–1081. https://doi.org/10.1029/WR017i004p01075

Brauchler, R., Liedl, R., & Dietrich, P. (2003). A travel time based hydraulic tomographic approach. *Water Resources Research*, *39*(12), 1370. https://doi.org/10.1029/2003WR002262

Cacas, M. C., Ledoux, E., de Marsily, G., Tillie, B., Barbreau, A., Durand, E., et al. (1990). Modeling fracture flow with a stochastic discrete fracture network: Calibration and validation. 1. The flow model. *Water Resources Research*, *26*(3), 479–489. https://doi.org/10.1029/WR026i003p00479

Castagna, M., Becker, M. W., & Bellin, A. (2011). Joint estimation of transmissivity and storativity in a bedrock fracture. *Water Resources Research*, *47*, W09504. https://doi.org/10.1029/2010WR009262

Dershowitz, W. S., & Einstein, H. H. (1988). Characterizing rock joint geometry with joint system models. *Rock Mechanics and Rock Engineering*, *21*(1), 21–51. https://doi.org/10.1007/bf01019674

Dershowitz, W. S., & Herda, H. H. (1992). Interpretation of fracture spacing and intensity.

Duguid, J. O., & Lee, P. C. Y. (1977). Flow in fractured porous-media. *Water Resources Research*, *13*(3), 558–566. https://doi.org/10.1029/WR013i003p00558

Dverstorp, B., Andersson, J., & Nordqvist, W. (1992). Discrete fracture network interpretation of field tracer migration in sparsely fractured rock. *Water Resources Research*, *28*(9), 2327–2343. https://doi.org/10.1029/92WR01182

Dykhuizen, R. C. (1990). A new coupling term for dual-porosity models. *Water Resources Research*, *26*(2), 351–356. https://doi.org/10.1029/WR026i002p00351

Farichah, H., Hsu, C., & Tien, Y. (2017). A novel equation to determine geometrical representative elementary volume of fractured rock mass. Paper presented at the 51st US Rock Mechanics/Geomechanics Symposium.
Fischer, P., Jardani, A., & Lecoq, N. (2018). Hydraulic tomography of discrete networks of conduits and fractures in a karstic aquifer by using a deterministic inversion algorithm. *Advances in Water Resources*, *112*, 83–94. https://doi.org/10.1016/j.advwatres.2017.11.029
Fischer, P., Jardani, A., Wang, X., Jourde, H., & Lecoq, N. (2017). Identifying flow networks in a karstified aquifer by application of the cellular automata-based deterministic inversion method (Lez aquifer, France). *Water Resources Research*, *53*, 10,508–10,522. https://doi.org/10.1002/2017WR020921
Gerke, H. H., & Vangenuchten, M. T. (1993a). A dual-porosity model for simulating the preferential movement of water and solutes in structured porous-media. *Water Resources Research*, *29*(2), 305–319. https://doi.org/10.1029/92WR02339
Gerke, H. H., & Vangenuchten, M. T. (1993b). Evaluation of a 1st-order water transfer term for variably saturated dual-porosity flow models. *Water Resources Research*, *29*(4), 1225–1238. https://doi.org/10.1029/92WR02467
Golder Associates Inc (2015). *Fracman7 interactive discrete feature data analysis, geometric modeling and exploration simulation, user documentation*. Redmond: Golder Associates Inc.
Grenon, M., & Hadjigeorgiou, J. (2012). Applications of fracture system models (fsm) in mining and civil rock engineering design. *International Journal of Mining Reclamation and Environment*, *26*(1), 55–73. https://doi.org/10.1080/17480930.2011.639190
Hao, Y., Yeh, T.-C. J., Xian, J., Illman, W. A., Ando, K., Hsu, K.-C., & Lee, C.-H. (2008). Hydraulic tomography for detecting fracture zone connectivity. *Ground Water*, *46*(2), 183–192. https://doi.org/10.1111/j.1745-6584.2007.00388.x
Huang, S.-Y., Wen, J.-C., Yeh, T.-C. J., Lu, W., Juan, H.-L., Tseng, C.-M., et al. (2011). Robustness of joint interpretation of sequential pumping tests: Numerical and field experiments. *Water Resources Research*, *47*, W10530. https://doi.org/10.1029/2011WR010698
Illman, W. A. (2014). Hydraulic tomography offers improved imaging of heterogeneity in fractured rocks. *Groundwater*, *52*(5), 659–684. https://doi.org/10.1111/gwat.12119
Illman, W. A., Berg, S. J., & Yeh, T.-C. J. (2012). Comparison of approaches for predicting solute transport: Sandbox experiments. *Ground Water*, *50*(3), 421–431. https://doi.org/10.1111/j.1745-6584.2011.00859.x
Illman, W. A., & Hughson, D. L. (2005). Stochastic simulations of steady state unsaturated flow in a three-layer, heterogeneous, dual continuum model of fractured rock. *Journal of Hydrology*, *307*(1–4), 17–37. https://doi.org/10.1016/j.jhydrol.2004.09.015
Illman, W. A., Liu, X., Takeuchi, S., Yeh, T.-C. J., Ando, K., & Saegusa, H. (2009). Hydraulic tomography in fractured granite: Mizunami underground research site, Japan. *Water Resources Research*, *45*, W01406. https://doi.org/10.1029/2007WR006715
Kuhlman, K. L., Hinnell, A. C., Mishra, P. K., & Yeh, T.-C. J. (2008). Basin-scale transmissivity and storativity estimation using hydraulic tomography. *Ground Water*, *46*(5), 706–715. https://doi.org/10.1111/j.1745-6584.2008.00455.x
Liu, S. Y., Yeh, T. C. J., & Gardiner, R. (2002). Effectiveness of hydraulic tomography: Sandbox experiments. *Water Resources Research*, *38*(4), 1034. https://doi.org/10.1029/2001WR000338
Liu, X., Illman, W. A., Craig, A. J., Zhu, J., & Yeh, T. C. J. (2007). Laboratory sandbox validation of transient hydraulic tomography. *Water Resources Research*, *43*, W05404. https://doi.org/10.1029/2006WR005144
Liu, Y., Hao, Y., Fan, Y., Wang, T., Huo, X., Liu, Y., & Yeh, T.-C. J. (2014). A nonstationary extreme value distribution for analysing the cessation of karst spring discharge. *Hydrological Processes*, *28*(20), 5251–5258. https://doi.org/10.1002/hyp.10013
Long, J. C. S., Remer, J. S., Wilson, C. R., & Witherspoon, P. A. (1982). Porous-media equivalents for networks of discontinuous fractures. *Water Resources Research*, *18*(3), 645–658. https://doi.org/10.1029/WR018i003p00645
Miller, I., Lee, G., & Dershowitz, W. (2001). *MAFIC matrix/fracture interaction code with heat and solute transport user documentation (version2.0)*. Redmond: Golder Associates Inc.
Moench, A. F. (1984). Double-porosity models for a fissured groundwater reservoir with fracture skin. *Water Resources Research*, *20*(7), 831–846. https://doi.org/10.1029/WR020i007p00831
National Research Council (1996). *Rock fractures and fluid flow: Contemporary understanding and applications*. Washington, DC: National Academy Press.
Neuman, S. P. (1987). Stochastic continuum representation of fractured rock permeability as an alternative to the rev and fracture network concepts. Paper presented at the Proc. of 28th US Rock Mechanics Symp, Tuscon, AZ.
Ni, C.-F., & Yeh, T.-C. J. (2008). Stochastic inversion of pneumatic cross-hole tests and barometric pressure fluctuations in heterogeneous unsaturated formations. *Advances in Water Resources*, *31*(12), 1708–1718. https://doi.org/10.1016/j.advwatres.2008.08.007
Pruess, K., & Narasimhan, T. N. (1985). A practical method for modeling fluid and heat-flow in fractured porous-media. *Society of Petroleum Engineers Journal*, *25*(01), 14–26. https://doi.org/10.2118/10509-pa
Reimus, P., Pohll, G., Mihevc, T., Chapman, J., Haga, M., Lyles, B., et al. (2003). Testing and parameterizing a conceptual model for solute transport in a fractured granite using multiple tracers in a forcedgradient test. *Water Resources Research*, *39*(12), 1356. https://doi.org/10.1029/2002WR001597
Roubinet, D., & Irving, J. (2014). Discrete-dual-porosity model for electric current flow in fractured rock. *Journal of Geophysical Research: Solid Earth*, *119*, 767–786. https://doi.org/10.1002/2013JB010668
Sharmeen, R., Illman, W. A., Berg, S. J., Yeh, T.-C. J., Park, Y.-J., Sudicky, E. A., & Ando, K. (2012). Transient hydraulic tomography in a fractured dolostone: Laboratory rock block experiments. *Water Resources Research*, *48*, W10532. https://doi.org/10.1029/2012WR012216
Tsang, Y. W., Tsang, C. F., Hale, F. V., & Dverstorp, B. (1996). Tracer transport in a stochastic continuum model of fractured media. *Water Resources Research*, *32*(10), 3077–3092. https://doi.org/10.1029/96WR01397
Tso, C.-H. M., Zha, Y., Yeh, T.-C. J., & Wen, J.-C. (2016). The relative importance of head, flux, and prior information in hydraulic tomography analysis. *Water Resources Research*, *52*, 3–20. https://doi.org/10.1002/2015wr017191
Wang, X., Jardani, A., & Jourde, N. (2017). A hybrid inverse method for hydraulic tomography in fractured and karstic media. *Journal of Hydrology*, *551*, 29–46. https://doi.org/10.1016/j.jhydrol.2017.05.051
Warren, J. E., & Root, P. J. (1963). The behavior of naturally fractured reservoirs. *Society of Petroleum Engineers Journal*, *3*(03), 245–255. https://doi.org/10.2118/426-pa
Wen, J.-C., Wu, C.-M., Yeh, T.-C. J., & Tseng, C.-M. (2010). Estimation of effective aquifer hydraulic properties from an aquifer test with multi-well observations (Taiwan). *Hydrogeology Journal*, *18*(5), 1143–1155. https://doi.org/10.1007/s10040-010-0577-1
Xiang, J., Yeh, T.-C. J., Lee, C.-H., Hsu, K.-C., & Wen, J.-C. (2009). A simultaneous successive linear estimator and a guide for hydraulic tomography analysis. *Water Resources Research*, *45*, W10532. https://doi.org/10.1029/2008WR007180
Ye, M., Khaleel, R., & Yeh, T. C. J. (2005). Stochastic analysis of moisture plume dynamics of a field injection experiment. *Water Resources Research*, *41*, W03013. https://doi.org/10.1029/2004WR003735
Yeh, T.-C., Khaleel, R., & Carroll, K. C. (2015). *Flow through heterogeneous geologic media*. New York: Cambridge University Press. https://doi.org/10.1017/CBO9781139879323

Yeh, T. C. J., Jin, M. H., & Hanna, S. (1996). An iterative stochastic inverse method: Conditional effective transmissivity and hydraulic head fields. *Water Resources Research*, *32*(1), 85–92. https://doi.org/10.1029/95WR02869

Yeh, T.-C. J., Mao, D.-q., Zha, Y.-y., Wen, J.-c., Wan, L., Hsu, K.-c., & Lee, C.-h. (2015). Uniqueness, scale, and resolution issues in groundwater model parameter identification. *Water Science and Engineering*, *8*(3), 175–194. https://doi.org/10.1016/j.wse.2015.08.002

Yeh, T.-C. J., Srivastava, R., Guzman, A., & Harter, T. (1993). A numerical-model for water-flow and chemical-transport in variably saturated porous-media. *Ground Water*, *31*(4), 634–644. https://doi.org/10.1111/j.1745-6584.1993.tb00597.x

Zha, Y. Y., Yeh, T. C. J., Illman, W. A., Tanaka, T., Bruines, P., Onoe, H., & Saegusa, H. (2015). What does hydraulic tomography tell us about fractured geological media? A field study and synthetic experiments. *Journal of Hydrology*, *531*, 17–30. https://doi.org/10.1016/j.jhydrol.2015.06.013

Zha, Y. Y., Yeh, T.-C. J., Illman, W. A., Tanaka, T., Bruines, P., Onoe, H., et al. (2016). An application of hydraulic tomography to a large-scale fractured granite site, Mizunami, Japan. *Groundwater*, *54*(6), 793–804. https://doi.org/10.1111/gwat.12421

Zha, Y. Y., Yeh, T.-C. J., Mao, D., Yang, J., & Lu, W. (2014). Usefulness of flux measurements during hydraulic tomographic survey for mapping hydraulic conductivity distribution in a fractured medium. *Advances in Water Resources*, *71*, 162–176. https://doi.org/10.1016/j.advwatres.2014.06.008

Zhang, H., & Thurber, C. H. (2007). Estimating the model resolution matrix for large seismic tomography problems based on Lanczos bidiagonalization with partial reorthogonalization. *Geophysical Journal International*, *170*(1), 337–345. https://doi.org/10.1111/j.1365-246X.2007.03418.x

Zhu, J. F., & Yeh, T. C. J. (2005). Characterization of aquifer heterogeneity using transient hydraulic tomography. *Water Resources Research*, *41*, W07028. https://doi.org/10.1029/2004WR003790

Zhu, J. F., & Yeh, T. C. J. (2006). Analysis of hydraulic tomography using temporal moments of drawdown recovery data. *Water Resources Research*, *42*, W02403. https://doi.org/10.1029/2005WR004309

Zimmerman, R. W., Chen, G., Hadgu, T., & Bodvarsson, G. S. (1993). A numerical dual-porosity model with the semianalytical treatment of fracture-matrix flow. *Water Resources Research*, *29*(7), 2127–2137. https://doi.org/10.1029/93WR00749